Accepted Article Preview: Published ahead of advance online publication

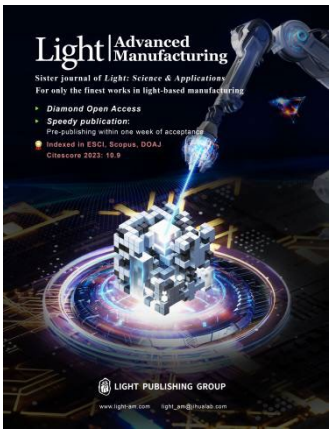

Disturbance-Introduced Interferometry: Surface Topography Metrology Beyond Vibration Isolation and Phase-Shifting Control

Lin Li, Rui Xu, Yawen He, Lihua Lei, Xinzhe Li, Lintong Du, Yue Pan, Yumai Ji, Yang Shen, Shuxin Liu, Sen Han and Jiamiao Yang.

Cite this article as: Lin Li, Rui Xu, Yawen He, Lihua Lei, Xinzhe Li, Lintong Du, Yue Pan, Yumai Ji, Yang Shen, Shuxin Liu, Sen Han and Jiamiao Yang. Disturbance-Introduced Interferometry: Surface Topography Metrology Beyond Vibration Isolation and Phase-Shifting Control. *Light: Advanced Manufacturing* accepted article preview 2 June 2026; doi: 10.37188/lam.2026.090

Received 10 March 2026; revised 30 May 2026; accepted 1 June 2026;
Accepted article preview online 2 June 2026

Disturbance-Introduced Interferometry: Surface Topography Metrology Beyond Vibration Isolation and Phase-Shifting Control

Lin Li[1,2,†], Rui Xu[3,4,†], Yawen He[1,2], Lihua Lei[5,6], Xinzhe Li[1,2], Lintong Du[1,2], Yue Pan[1,2], Yumai Ji[1,2], Yang Shen[1,2], Shuxin Liu[1,2,7], Sen Han[8,9] and Jiamiao Yang[1,2,7,*]

[1] School of Automation and Intelligent Sensing, Shanghai Jiao Tong University, Shanghai, 200240, China

[2] State Key Laboratory of Submarine Geoscience, School of Electronic Information and Electrical Engineering, Shanghai Jiao Tong University, 200240 Shanghai, China

[3] State Key Laboratory of Dynamic Optical Imaging and Measurement, Changchun Institute of Optics, Fine Mechanics and Physics, Chinese Academy of Sciences, Changchun 130033, China

[4] University of Chinese Academy of Sciences, Beijing 100049, China

[5] Shanghai Institute of Measurement and testing Technology Co., Ltd., Shanghai 201203, China

[6] Shanghai Key Laboratory of Online Test and Control Technology, Shanghai 201203, China

[7] Institute of Medical Robotics, Shanghai Jiao Tong University, Shanghai 200240, China

[8] School of Optical-Electrical and Computer Engineering, University of Shanghai for

Science and Technology, Shanghai 200093, China.

[9] Suzhou H&L Instruments LLC, Suzhou 215123, China.

* jiamiaoyang@sjtu.edu.cn

† These authors contributed equally to this work.

Abstract

Phase-shifting interferometry underpins surface topography metrology in precision fields such as semiconductor manufacturing and optical engineering. However, its reliance on stringent vibration isolation and precise phase-shifting control restricts its applicability in many scenarios, particularly in the characterisation of large-aperture optical components. To address these limitations, we present disturbance-introduced interferometry, which harnesses ambient random mechanical disturbances as phase-shifting sources. We also develop a large-disturbance-adaptive natural phase decoding algorithm to reconstruct the surface topography from the resulting interferograms. This framework reduces reliance on stringent vibration isolation and precise phase-shifting control, making it particularly suitable for large-aperture surface metrology and measurements in vibration-prone manufacturing environments. Experimental results demonstrated that even in uncontrolled and vibration-prone environments, the method achieves a root-mean-square wavefront repeatability below $0.0018\,\lambda$. These measurements closely agree with those from conventional phase-shifting interferometry in strictly controlled settings, with root-mean-square differences of $0.0002\,\lambda$ for spherical surfaces and $0.0007\,\lambda$ for planar surfaces and peak-to-valley differences of $0.0043\,\lambda$ and $0.0038\,\lambda$, respectively. In contrast, conventional phase-shifting interferometry fails to deliver reliable measurements under such dynamically disturbed conditions.

Keywords: Phase-shifting interferometry, Surface metrology, Vibration insensitivity

Introduction

Optical interferometry[1-3] is widely used for surface metrology, with phase-shifting interferometry[4-10] (PSI) being considered the 'gold standard' for measuring surface form and texture. To achieve increasingly precise measurements, researchers have consistently pushed the boundaries of hardware capabilities and environmental conditions[11-20]. This has resulted in an inherent escalation in system complexity and costs. Furthermore, as many of these strategies approach their theoretical limits, further improvements become increasingly difficult to achieve[21-23]. Among these challenges, vibration isolation and phase-shifting control have long been the focus of researchers because they directly affect the accuracy and stability of measurements[24-27].

Various passive and active vibration isolation techniques have been employed to reduce the undesired phase difference between reference and test beams[28-31]. These strategies suppress transmitted environmental disturbances, but they do not correct phase-shifting errors or completely remove residual perturbations by themselves. Many phase-shifting techniques have also been developed, including mechanical phase shifters[32, 33], modulating polarization[14, 18], wavelength modulation[16], displacing a grating[34, 35], and tilting a parallel plate. For example, Ref. 32 reported a high-precision large-aperture differential confocal-interferometric method that uses the mechanical phase shifting of a heavy-load reference lens to achieve high-stability surface-profile measurements. However, this approach still relies on dedicated phase-shifting hardware and the precise control of a heavy-load reference element, which increases the system complexity and cost. Ref. 36 applied polarization phase shifting to large-aperture dynamic interferometry but also showed that stress-induced birefringence in large optics introduces polarisation aberrations into the measured wavefront. These errors are not inherently removed by the phase-shifting process and, therefore, require additional characterisation and correction. These challenges are particularly severe for large-aperture components[32, 36, 37], in which longer measurement cavity lengths and larger test surfaces amplify the effects of vibrations and phase errors. Satisfying stringent

performance specifications poses significant challenges, often making the manufacturing of such devices impractical.

Spatial carrier techniques[38-40] are resilient to vibrations and do not require sequential phase shifting; however, they sacrifice spatial resolution and may introduce retrace errors because carrier fringes must be generated by tilting the optical elements. Recently, a deep-learning-based high-precision large-aperture single-frame interferometric method was developed[41]; it enables rapid surface-profile reconstruction without a phase shifter. Although promising, this method relies on model training using small-aperture measurements and an aperture-expansion system. Therefore, its broader generalisation across different components and system configurations remains to be further validated. Another class of approaches, referred to as model-based PSI[42-51] or self-calibration methods[52-54], is currently considered promising. For example, an advanced iterative algorithm (AIA)[44] was developed to simultaneously estimate phase distribution and phase steps. Subsequently, an iterative phase-shifting algorithm[48,51] extended this approach to accommodate minor random tilts. Although these methods can adaptively estimate unknown phase shifts, they fail when the disturbance-induced tilt exceeds one wavelength. Therefore, they currently serve only as supplementary tools when vibration isolation is suboptimal and remain dependent on environmental control and precise phase-shifting equipment.

Because vibrations and phase-shifting errors are inherently difficult to isolate completely, we adopt a counterintuitive strategy: rather than suppressing these disturbances, they are exploited. This approach has resulted in disturbance-introduced interferometry (DII). DII harnesses ambient random mechanical disturbances (RMDs), such as structural vibration or deformation, to naturally encode the measured phase information into interference patterns. RMDs are reconceptualised as beneficial excitation signals rather than detrimental noise, thereby eliminating the need for conventional phase-shifting mechanisms or vibration isolation systems. We present a natural phase decoding algorithm (NPDA) for collecting and analysing interferograms

under disturbance conditions. By employing a coarse-to-fine approach and iteratively updating decoupled spatiotemporal variables, the NPDA accurately extracts phase information from interference patterns and adapts to significant disturbances. DII enables nanoscale surface-topography measurements.

Basics

Principle of DII

As illustrated in Fig. 1 and Supplementary Movie S1, DII involves light from a laser passing through a beam-expanding system to a partially reflective reference surface. At this surface, the incident light is split into two portions: the reflected portion serves as the reference beam, whereas the transmitted portion propagates through the measurement cavity, reflects off the test surface, and returns as the test beam. The two beams are then recombined via the beam-expanding system and imaging lens to form interferometric images at the camera plane. RMDs alter the relative positions of the test and reference surfaces by dynamically modulating the optical path difference between the test and reference beams. This process naturally encodes the interferometric images using RMDs. DII captures these disturbance-modulated interferometric images and subsequently analyses them using the NPDA to decode the interferometric phase and reconstruct the test surface topography.

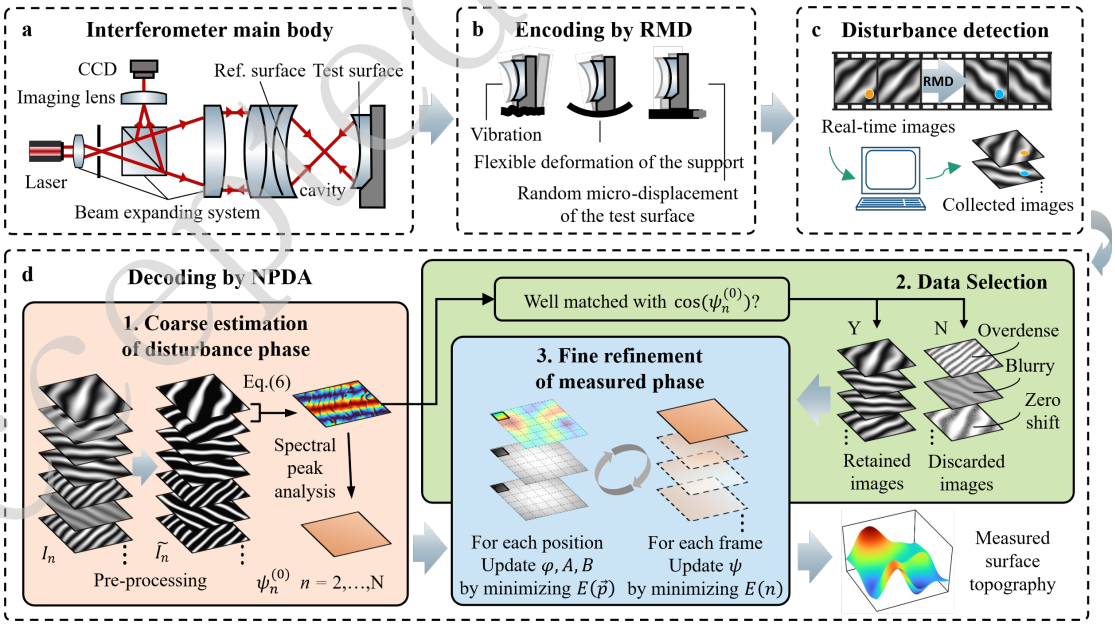

Fig. 1 Schematic of disturbance-introduced interferometry (DII). a Interferometer main body. **b** Phase information is encoded into the interference patterns via random mechanical disturbances (RMDs), including vibration, support flexible deformation, and random micro-displacement. **c**

Sequential acquisition of interference images under various disturbance conditions. **d** Extraction of the embedded phase information from the recorded interference patterns through the natural phase decoding algorithm (NPDA).

In DII, RMDs can be introduced passively or actively via vibration, flexible deformation of the support, or random micro-displacement of the test surface. The theoretical interferometric intensity is first described by the standard interference model[48]:

$$I_n^t(\vec{p}) = A(\vec{p}) + B(\vec{p})\cos\left[\phi(\vec{p}) + \psi_n(\vec{p})\right] \quad [1]$$

where $I_n^t(\vec{p})$ is the intensity at pixel $\vec{p} = (x, y)$ at time n; A, B, ϕ, and ψ represent the background intensity, modulation amplitude, measured phase, and disturbance-induced phase-shift, respectively. In DII, A, B, and ϕ are considered to be time-invariant, consistent with conventional PSI. Following the widely adopted formulation in tilt PSI[48, 51], the disturbance phase is defined as

$$\psi_n(\vec{p}) = d_n + k_{xn}x + k_{yn}y \quad [2]$$

where d_n is the parallel phase shift, and k_{xn}, k_{yn} are the tilt gradients along the x and y axes, respectively.

To achieve robust performance against significant disturbances while maintaining high precision, the proposed NPDA employs a three-stage coarse-to-fine strategy. In the initial stage, termed the 'coarse estimation of disturbance phase', a rapid framewise global estimation of the temporal disturbance variables k_{xn}, k_{yn}, and d_n is performed to obtain their initial values for subsequent refinement. This stage is characterised by the use of spectral analysis to effectively separate the signal from noise. The chirp Z-transform (CZT) is employed to further enhance the resolution of this parameter estimation, enabling a swift yet effective initial assessment. In the second stage, 'data selection', a quality control mechanism is implemented to filter the results from the coarse estimation. This process assesses both the interferograms and their

corresponding initial estimates, discarding low-quality data and unreliable results. The refined dataset, now comprising high-quality interferograms and reliable initial parameters, proceeds to the final 'fine refinement' stage. The spatial and temporal variables are decoupled and iteratively optimised. This optimisation process seeks to minimise the spatial loss function, $E(\vec{p})=\sum_{n=1}^{N}\left(I_n^t(\vec{p})-I_n(\vec{p})\right)^2$, to update the parameters $A(\vec{p}), B(\vec{p})$ and a temporal loss function, $E(n)=\sum_{\vec{p}=\vec{p}_1}^{\vec{p}_M}\left(I_n^t(\vec{p})-I_n(\vec{p})\right)^2$, to update the frame-specific disturbance parameters $\phi(\vec{p})$ and d_n, k_{xn}, k_{yn}. This iterative process is continued until convergence is achieved. Finally, the topographic reconstruction is completed through phase unwrapping and unit conversion of the refined phase map ϕ.

Coarse estimation of the disturbance phase

Image preprocessing

Image preprocessing is employed to eliminate the effects of the background intensity A, modulation amplitude B, and phase ϕ, yielding an estimated normalized interference image $I_n^{\%}(\vec{p})$ that approximates $\cos\left[\phi(\vec{p})+\psi_n(\vec{p})\right]$.

$$A_{\text{est}}=\frac{1}{2}\left[\text{LPF}\left(\max_n\{I_n\}_{n=1}^{N}\right)+\text{LPF}\left(\min_n\{I_n\}_{n=1}^{N}\right)\right] \quad [3]$$

$$B_{\text{est}}=\frac{1}{2}\left[\text{LPF}\left(\max_n\{I_n\}_{n=1}^{N}\right)-\text{LPF}\left(\min_n\{I_n\}_{n=1}^{N}\right)\right] \quad [4]$$

$$I_n^{\%}=\frac{I_n-A_{\text{est}}}{B_{\text{est}}} \quad [5]$$

Here, n denotes the frame index of the interference image, N is the total number of images used in the computation, A_{est} and B_{est} are the estimated values of A and B, respectively, and $\text{LPF}(\cdot)$ represents a low-pass filtering operation.

Calculation of disturbance phase parameters

For any point $\vec{p}$ and its neighbouring point $\vec{p}'$, we assume $\cos(\psi_n(\vec{p})) \approx \cos(\psi_n(\vec{p}'))$. By defining $\alpha_n = \cos(\psi_n)$, the following relationship is derived:

$$\begin{aligned}\alpha_n &= \frac{I_1(\vec{p})^2 - I_1(\vec{p}')^2 + I_n(\vec{p})^2 - I_n(\vec{p}')^2}{2\left(I_1(\vec{p})I_n(\vec{p}) - I_1(\vec{p}')I_n(\vec{p}')\right)} \\ &= \frac{e^{i\left(k_{xn}x+k_{yn}y+d_n\right)} + e^{-i\left(k_{xn}x+k_{yn}y+d_n\right)}}{2}\end{aligned} \quad [6]$$

The disturbance phase parameters k_{xn}, k_{yn}, and d_n are then calculated through the following steps:

$$\Phi_n(\omega_x, \omega_y) = \mathrm{CZT}\{\alpha_n(x, y)\}(\omega_x, \omega_y) \quad [7]$$

$$(k_{xn}, k_{yn}) = \arg\max_{(\omega_x, \omega_y)} \left|\Phi_n(\omega_x, \omega_y)\right| \quad [8]$$

$$\mathbf{D} = \begin{bmatrix} -\sin\left((k_{xn}, k_{yn}) \cdot \vec{p}_1\right) & \cos\left((k_{xn}, k_{yn}) \cdot \vec{p}_1\right) \\ \vdots & \vdots \\ -\sin\left((k_{xn}, k_{yn}) \cdot \vec{p}_M\right) & \cos\left((k_{xn}, k_{yn}) \cdot \vec{p}_M\right) \end{bmatrix} \quad [9]$$

$$\{\mathbf{u}\} = \begin{bmatrix} \alpha_n(\vec{p}_1) \\ \vdots \\ \alpha_n(\vec{p}_M) \end{bmatrix} \quad [10]$$

$$\{\mathbf{v}\} = \begin{bmatrix} v_1 \\ v_2 \end{bmatrix} = [\mathbf{D}]^{-1}\{\mathbf{u}\} \quad [11]$$

$$d_n = \tan^{-1}\left(-\frac{v_1}{v_2}\right) \quad [12]$$

Here, CZT refers to the chirp-Z transform, which enhances the resolution of the initial estimates $k_{xn}^{(0)}$ and $k_{yn}^{(0)}$ (see Supplementary Note 1).

Resolving spectral ambiguity

Owing to the presence of two conjugate peaks in the spectrum of α_n, an ambiguity occurs in the disturbance phase parameters across different frames. This is addressed as follows: We define $\beta_n = \sin(\psi_n)$ and compute

$$\mathrm{W}\left[\phi_n(\vec{p})^t\right] = \arctan\left[\frac{\mathrm{sign}\left(\beta_n^t(\vec{p})\right)\times\left(\alpha_n^t(\vec{p})I_1(\vec{p}) - I_n(\vec{p})\right)}{\mathrm{sign}\left(\beta_n^t(\vec{p})\right)\times\beta_n^t(\vec{p})I_1(\vec{p})}\right], \quad n = 2,3,\ldots,N \quad [13]$$

where W denotes 2π -phase wrapping. If

$$\sum_{\vec{p}}\left(\mathrm{W}\left[\phi_n(\vec{p})^t\right] - \mathrm{W}\left[\phi_2(\vec{p})^t\right]\right)^2 > \sum_{\vec{p}}\left(\mathrm{W}\left[\phi_n(\vec{p})^t\right] + \mathrm{W}\left[\phi_2(\vec{p})^t\right]\right)^2 \quad [14]$$

then the parameters are adjusted by setting $k_{xn} = -k_{xn}$, $k_{yn} = -k_{yn}$, and $d_n = -d_n$ to resolve the ambiguity.

Note that this step only resolves the inter-frame ambiguity, ensuring consistent phase signs across different frames. However, it does not determine the absolute orientation of the measured surface. Resolving the surface sign ambiguity would require additional constraints, such as knowledge of the tilt disturbance direction.

Data Selection

Because our method is based on DII, the occurrence of non-ideal or low-quality interferograms (‘dirty data’) is an expected part of the data acquisition process. These low-quality frames typically fall into two categories.

1. Over-dense fringes: An excessive disturbance amplitude at a given moment can cause the test component to deviate significantly from its ideal position, thereby introducing substantial tracking errors. This manifests as overly dense interference fringes.

2. Blurred fringes: High disturbance frequency can cause the interference pattern to shift significantly during camera exposure, resulting in a blurred image owing to motion artefacts.

To ensure the robustness and accuracy of the final measurements, we introduce a 'data selection' mechanism. This mechanism automatically identifies and filters out low-quality frames by evaluating a quality index (QI) of each interferogram. The QI is defined based on the mean squared error (MSE) between the cosine of the estimated disturbance phase $\cos(d_n^{(0)} + k_{xn}^{(0)}x + k_{yn}^{(0)}y)$ and that of the directly computed normalised interference pattern ($\cos(\psi_n)$ from Eq. (3)). A higher QI value indicates a better match and thus higher confidence in the data and initial estimate. This mechanism serves the dual purpose of rejecting poor-quality interferograms and filtering out unreliable results from the coarse estimation stage.

The effectiveness of this mechanism was demonstrated in a simulation, shown in Fig. 2. In this example, ten interferograms were processed. Among them, frame I_2 was synthetically blurred to simulate high-frequency vibrations, whereas frame I_3 was given a large tilt coefficient to simulate over-dense fringes from excessive displacement. The plot in Fig. 2b compares the calculated QI for each frame with the reciprocal of the ground-truth estimation error (1/Err), where Err is the RMSE between the estimated disturbance phase and its known true value.

The results clearly showed a strong correlation between the QI and 1/Err, confirming that the QI is an effective predictor of coarse estimation accuracy. By applying a simple QI threshold (e.g. 0.5), low-quality frames with blurry (I_2) and over-dense (I_3) fringes were successfully identified and discarded. This validation demonstrated the effectiveness of the data selection mechanism in automatically ensuring that only high-quality data proceeds to the fine refinement stage.

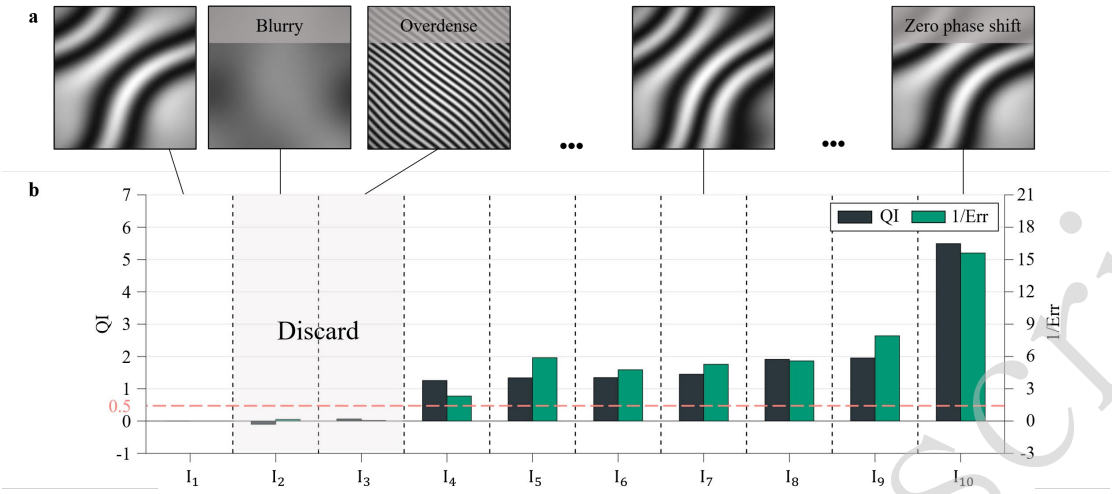

Fig. 2 Validation of the data selection mechanism using the quality index (QI). **a** Sequence of ten simulated interferograms, sorted by their calculated QI values in ascending order. The set includes deliberately corrupted frames, such as a blurred image (I_2) simulating high-frequency disturbances and an over-dense image (I_3) simulating excessive disturbance amplitude. A frame with zero phase shift (I_{10}) is also included for comparison. **b** Plot comparing the QI of each frame against the reciprocal of the ground-truth estimation error (1/Err). The strong correlation demonstrates that the QI is an effective predictor of estimation accuracy. By applying a simple threshold (e.g. QI > 0.5, indicated by the red dashed line), low-quality frames (I_2 and I_3) are successfully identified and discarded.

Fine refinement of the measured phase

The coarse estimation stage relies on rough approximations, resulting in suboptimal precision that necessitates further refinement. The disturbance phase parameters obtained from the coarse estimation—denoted as $d_n^{(0)}$, $k_{xn}^{(0)}$, and $k_{yn}^{(0)}$—and the corresponding disturbance phase $\psi^{(0)}$ serve as initial values for the fine refinement stage.

Because the measured phase ϕ and disturbance phase ψ are coupled within the cosine function, decoupling them is critical for accurate computation. To achieve this,

we employ an iterative strategy separating spatial and temporal variables, consisting of the following two steps, which is an extension of the AIA[44]:

Pointwise update of spatial variables A, B, and ϕ

We define $a(\vec{p}) = A(\vec{p})$, $b(\vec{p}) = B(\vec{p})\cos\phi(\vec{p})$, and $c(\vec{p}) = -B(\vec{p})\sin\phi(\vec{p})$. The theoretical intensity is expressed as

$$I_n^t(\vec{p}) = a(\vec{p}) + b(\vec{p})\cos\psi_n(\vec{p}) + c(\vec{p})\sin\psi_n(\vec{p}) \quad [15]$$

The loss function is defined as

$$\begin{aligned} E(\vec{p}) &= \sum_{n=1}^{N}\left(I_n^t(\vec{p}) - I_n(\vec{p})\right)^2 \\ &= \sum_{n=1}^{N}\left(a(\vec{p}) + b(\vec{p})\cos\psi_n(\vec{p}) + c(\vec{p})\sin\psi_n(\vec{p}) - I_n(\vec{p})\right)^2 \end{aligned} \quad [16]$$

where I_n^t is the theoretical interference image intensity, and I_n is the actual acquired intensity. Fixing $\psi_n = \psi_n^{(t-1)}$ (where t denotes the iteration round), the parameters $a(\vec{p})$, $b(\vec{p})$, and $c(\vec{p})$ are solved using the least squares method by setting

$$\frac{\partial E(\vec{p})}{\partial a(\vec{p})} = 0, \quad \frac{\partial E(\vec{p})}{\partial b(\vec{p})} = 0, \quad \frac{\partial E(\vec{p})}{\partial c(\vec{p})} = 0 \quad [17]$$

This can be reformulated as

$$\{R\} = [Q]^{-1}\{P\} \quad [18]$$

where

$$[Q] = \begin{bmatrix} N & \sum_{n=1}^{N}\cos\psi_n(\vec{p}) & \sum_{n=1}^{N}\sin\psi_n(\vec{p}) \\ \sum_{n=1}^{N}\cos\psi_n(\vec{p}) & \sum_{n=1}^{N}\cos^2\psi_n(\vec{p}) & \sum_{n=1}^{N}\cos\psi_n(\vec{p})\sin\psi_n(\vec{p}) \\ \sum_{n=1}^{N}\sin\psi_n(\vec{p}) & \sum_{n=1}^{N}\sin\psi_n(\vec{p})\cos\psi_n(\vec{p}) & \sum_{n=1}^{N}\sin^2\psi_n(\vec{p}) \end{bmatrix} \quad [19]$$

$$\{R\} = \begin{bmatrix} a(\vec{p}) \\ b(\vec{p}) \\ c(\vec{p}) \end{bmatrix} \quad [20]$$

$$\{P\} = \begin{bmatrix} \sum_{n=1}^{N} I_n(\vec{p}) \\ \sum_{n=1}^{N} I_n(\vec{p}) \cos\psi_n(\vec{p}) \\ \sum_{n=1}^{N} I_n(\vec{p}) \sin\psi_n(\vec{p}) \end{bmatrix} \quad [21]$$

From the solved $\{ R \}$, the updated variables are computed as

$$A(\vec{p}) = a(\vec{p}) \quad [22]$$

$$B(\vec{p}) = \sqrt{b(\vec{p})^2 + c(\vec{p})^2} \quad [23]$$

$$\phi(\vec{p}) = \tan^{-1}\left(-\frac{c(\vec{p})}{b(\vec{p})}\right) \quad [24]$$

After iterating over all pixels, the updated $A^{(t)}$, $B^{(t)}$, and $\phi^{(t)}$ are obtained.

Framewise update of temporal variables k_{xn}, k_{yn}, and d_n

The loss function is defined as

$$\begin{aligned} E_n &= \sum_{\vec{p}=\vec{p}_1}^{\vec{p}_M} \left(I_n^t(\vec{p}) - I_n(\vec{p})\right)^2 \\ &= \sum_{\vec{p}=\vec{p}_1}^{\vec{p}_M} \left(A(\vec{p}) + B(\vec{p})\cos\left(\phi(\vec{p}) + k_{xn}x + k_{yn}y + d_n\right) - I_n(\vec{p})\right)^2 \end{aligned} \quad [25]$$

Fixing $A(\vec{p}) = A^{(t)}(\vec{p})$, $B(\vec{p}) = B^{(t)}(\vec{p})$, and $\phi(\vec{p}) = \phi^{(t)}(\vec{p})$, the Levenberg–Marquardt (LM) algorithm[55] within nonlinear least squares is used to iteratively optimise k_{xn}, k_{yn}, and d_n. The parameter vector is defined as

$$\mathbf{C}_n = \begin{bmatrix} d_n \\ k_{xn} \\ k_{yn} \end{bmatrix} \quad [26]$$

The residual is

$$r(\mathbf{p}) = I_n(\mathbf{p}) - \left[A(\mathbf{p}) + B(\mathbf{p}) \cos\left(\phi(\mathbf{p}) + k_{xn}x + k_{yn}y + d_n \right) \right] \quad [27]$$

The Jacobian matrix is

$$J(\mathbf{p}) = \frac{\partial r(\mathbf{p})}{\partial \mathbf{C}_n} = B(\mathbf{p}) \sin\left(\phi(\mathbf{p}) + k_{xn}x + k_{yn}y + d_n \right) \begin{bmatrix} 1 \\ x \\ y \end{bmatrix} \quad [28]$$

The Hessian matrix and gradient are approximated as $H = J^T J$ and $g = J^T r$, respectively. The parameters are updated using

$$\mathbf{C}_n \leftarrow \mathbf{C}_n - (H + \lambda I)^{-1} g \quad [29]$$

The iterative procedure alternates between updating the spatial variables $A(\mathbf{p}), B(\mathbf{p})$, and $\phi(\mathbf{p})$ and refining the temporal parameters d_n, k_{xn}, and k_{yn} for each frame ($n = 2,3,\ldots,N$). Convergence in the temporal update is defined by the relative change in the norm of the parameter vector. Specifically, if

$$\frac{\left\| \mathbf{P}^{(t)} \right\| - \left\| \mathbf{P}^{(t-1)} \right\|}{\left\| \mathbf{P}^{(t)} \right\|} < \text{ò} \quad [30]$$

where $\mathbf{P}^{(t)} = \left[k_{xn}^{(t)}, k_{yn}^{(t)}, d_n^{(t)} \right]^T$ and ò is typically set to 10^{-6}, the iteration is terminated. Otherwise, the process continues until either this criterion is satisfied or the maximum number of iterations (set to 100) is reached. If the criterion is still not satisfied at the 100th iteration, the temporal refinement is terminated, and the current estimate is retained as the output of that update.

Numerical validation of DII under RMD conditions

To assess the effectiveness of DII, we conducted numerical simulations using MATLAB to model the measurement of a flat mirror. The interferograms were generated according to Eq. (1). Here, the background intensity and modulation amplitude were generated by the function $A(x,y) = B(x,y) = \exp(\log(0.75) \times (x^2 + y^2))$. The mirror surface, modelled by ϕ, was generated using a peaks function with a PV value of π rad, where the wavelength was 640 nm. The RMD was implemented by simulating the spatial deviations of the test element relative to its ideal position. These deviations encompassed six degrees of freedom, comprising translations and rotations along the x, y, and z axes. For each degree of freedom, the perturbation was modelled as a simple harmonic motion with an amplitude of $\pm 2\lambda$ and a frequency of 15 Hz. The simulated camera sampling frequency was 200 Hz. The disturbance phase ψ was obtained by calculating the offset distance along the optical axis at each sampling instant and applying a unit scaling of $4\pi/\lambda$. Additionally, white noise was incorporated into the interferograms to yield an image signal-to-noise ratio of 40 dB. Under these conditions, the disturbance phase amplitude (DPA)—defined as the maximum PV value of the nonlinear phase shift induced in the measurement cavity (see Supplementary Note 3)—reached approximately 7π rad. This DPA of 7π rad is a typical value under uncontrolled, vibration-prone environments, corresponding to a tilt of 3.5λ. For comparison, conventional four-step PSI (4-PSI) was also simulated under two disturbance regimes: strong (DPA = 7π rad) and weak (DPA = 7/100π rad).

The results are shown in Fig. 3, where the DII yielded a remarkably low RMSE of $0.0005\ \lambda$ (Fig. 3a), whereas 4-PSI produced an RMSE of $0.5\ \lambda$ under strong disturbances and $0.006\ \lambda$ under weak disturbances. Notably, even under weak disturbances, the RMSE of 4-PSI was more than one order of magnitude higher than

that of DII under strong disturbances. These results underscore the robustness of DII for high-precision surface metrology, maintaining accuracy even when the disturbance levels exceed the tolerance of conventional 4-PSI by more than 100-fold.

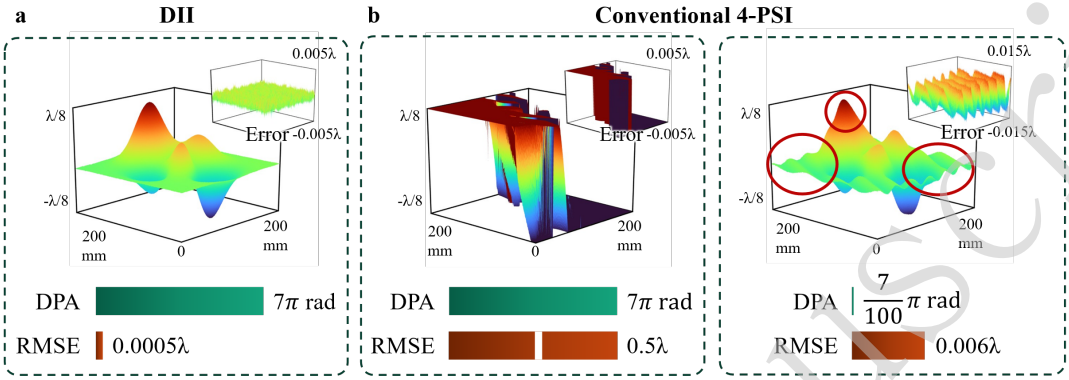

Fig. 3 Numerically simulated surface topography measurements of a planar component. a DII performance under a strong disturbance characterized by a disturbance phase amplitude (DPA) of 7π rad. **b** Conventional four-step PSI (4-PSI) results under differing disturbance conditions: strong disturbance (left panel) and weak disturbance (right panel, with DPA = 7/100π rad).

Robustness of DII against nonlinear disturbances

We assessed the robustness of the DII method against nonlinear disturbances by testing it across DPAs ranging from 0.01π rad to 12π rad. For comparison, we also evaluated three established anti-vibration techniques widely used in PSI: Hariharan's five-step algorithm (5-PSI), the AIA[44], and the general iterative algorithm[48] (GIA). Test surfaces, with a peak-to-valley height of λ/2, were generated by filtering Gaussian-distributed Fourier spectra. Each test involved five simulated interferograms with nominal phase shifts of 0, π/2, π, 3π/2, and 2π rad, perturbed by random tilts spanning the specified DPA range. Although DII can resolve unknown phase shifts, unlike 5-PSI, we used all methods with ideal phase shifts for equitable comparison.

Performance was assessed using 100 surface samples per DPA level, based on two metrics: the solution success rate (SSR), defined as the percentage of trials where the RMSE of the reconstructed surface was below 0.003λ, and the tolerable DPA, the maximum DPA permitting an SSR ≥ 80%. This 80% cutoff was used as an empirical comparison benchmark rather than a physical boundary. This provided a single, moderately stringent criterion for summarising the SSR–DPA curves and comparing the robustness of different methods under the same standard. The main robustness trends were still determined by the full SSR–DPA curves, whereas the tolerable DPA served only as a compact summary metric. These metrics were used to assess the robustness of each method in maintaining reconstruction precision under varying disturbance levels.

As shown in Fig. 4a, DII exhibited exceptional robustness, maintaining an SSR greater than 90% across the full DPA range. Conversely, conventional PSI methods degraded rapidly at lower disturbance levels, with the GIA being the most resilient, failing beyond 0.5π rad. Remarkably, although our tests capped the DPA at 12π rad, the capability of DII likely extends further. However, beyond this threshold, other error sources such as tracking errors would likely dominate the reconstruction, justifying our

range limit. This limit depends on the specific system and the measured object. Fig. 4b shows that the tested 12π-rad threshold reflected a disturbance tolerance 20 times greater than that of the GIA (0.6π rad) and 120 and 60 times greater than those of the 5-PSI and AIA, respectively. However, subsequent experiments confirmed that a 12π-rad disturbance level satisfies practical application requirements.

These findings demonstrate that DII reliably delivers sub-0.003 λ precision across a wide range of nonlinear disturbances, where conventional methods become ineffective, extending the practical limits far beyond what was previously achievable by PSI. Among the conventional methods, GIA exhibited the strongest anti-vibration capability. Thus, it was selected as the benchmark for subsequent experimental comparisons.

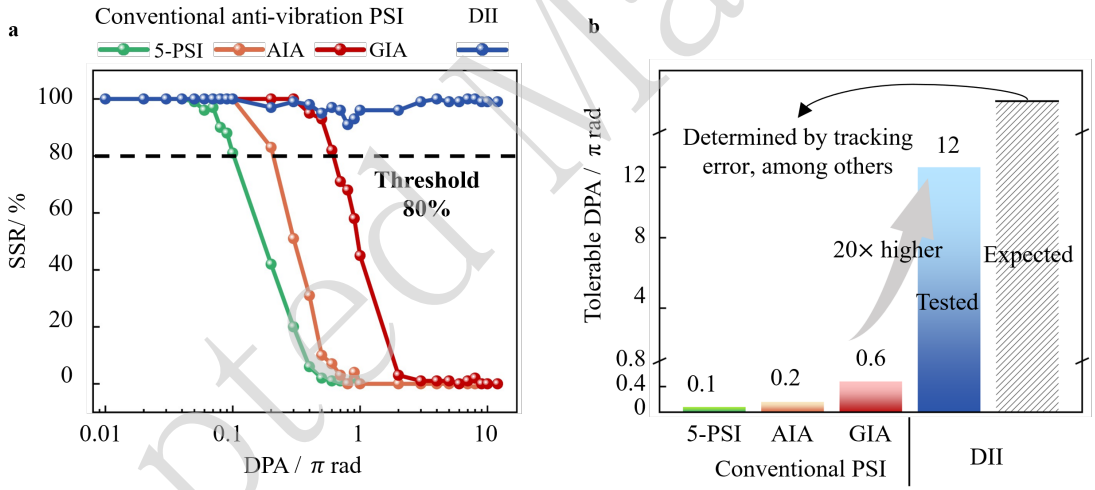

Fig. 4 Robustness comparison of methods under nonlinear disturbances. a Evaluation of the solution success rate (SSR) for the tested methods under DPAs ranging from 0.01π rad to 12π rad. **b** Assessment of the maximum tolerable DPA for each method.

Experimental setup and characterization

To validate DII, we developed a Fizeau-type interferometric prototype to measure the optical surface topography. The optical configuration is depicted in Fig. 5a, and the physical setup is shown in Fig. 5b. A 640 nm laser was coupled to an optical fibre (OF),

emerging as a divergent beam. This beam passed through a half-wave plate (HWP), stop plate (S), polarising beam splitter (PBS), quarter-wave plate (QWP), plate beam splitter (BS), and large-aperture collimator (LAC) to form a parallel beam. The HWP aligned the polarisation of the beam with the S-polarisation of the PBS for full reflection. The beam split at the reference lens (RL): one part reflected as the reference beam, and the other transmitted and reflected off the tested lens (TL) as the measurement beam. Both lenses were aligned using a precision adjustment mechanism (PAM). Returning light partially entered an alignment module (AAM) for the initial positioning via a charge-coupled device (CCD), whereas the remainder passed through the PBS, reflective mirror (RM), pinhole (P), and small-aperture collimator (SAC). Interference occurred at a rotating ground glass (RGG), captured by a CCD through an imaging lens (IL). All experiments were conducted following a rigorous and standardised internal laboratory protocol, identical to the operational procedures for industry-standard interferometers (e.g. Zygo), to ensure repeatability and validity of the results.

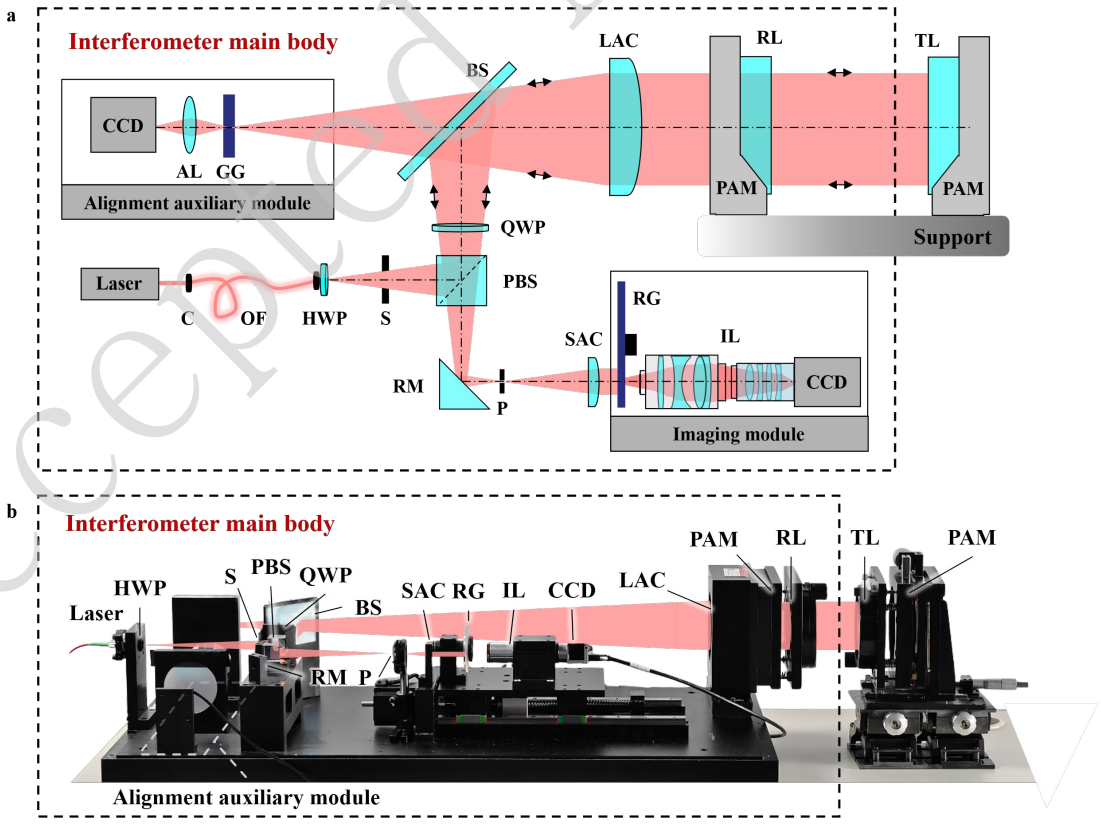

Fig. 5 Optical path diagram (a) and physical setup (b) for DII.

We assessed the performance of DII against conventional PSI using a plano-convex lens (effective aperture: 50.8 mm; curvature radius: 64.4 mm). DII experiments were conducted on a standard office desk without vibration isolation, intentionally introducing external vibrations through floor stomping. Conventional PSI experiments, which served as a reference, employed an air-floating vibration isolation platform (AFVI; model ZDT-P-MOT-F, Jiangxi Liansheng Technology Co., Ltd.) and a nanometre high-precision phase shifter (HPPS; model P77.S106, Coremorrow) controlled by piezoelectric ceramics.

The results, illustrated in Fig. 6, demonstrated a strong agreement between DII (Fig. 6b) and conventional PSI (Fig. 6c), with the cross-sectional profiles and surface quality metrics (root mean square, RMS; peak-to-valley, PV) aligned in Fig. 6d. For the spherical surface, DII yielded RMS = 0.0077 λ and PV = 0.0511 λ, which closely matched the conventional PSI values (RMS = 0.0079 λ and PV = 0.0554 λ). For the planar surface, the DII measurements (RMS = 0.6305 λ, PV = 2.3222 λ) were closely aligned with the PSI measurements (RMS = 0.6312 λ, PV = 2.3260 λ). Differences in the RMS and PV were minimal (order of 0.0001 λ and 0.001 λ, respectively), demonstrating the precision of DII matches that of PSI, despite lacking isolation or a dedicated phase shifter.

These findings highlight the robustness of DII against vibrations, enabling accurate topographic measurements of optical surfaces under minimal control, and rivalling the performance of PSI under optimised conditions.

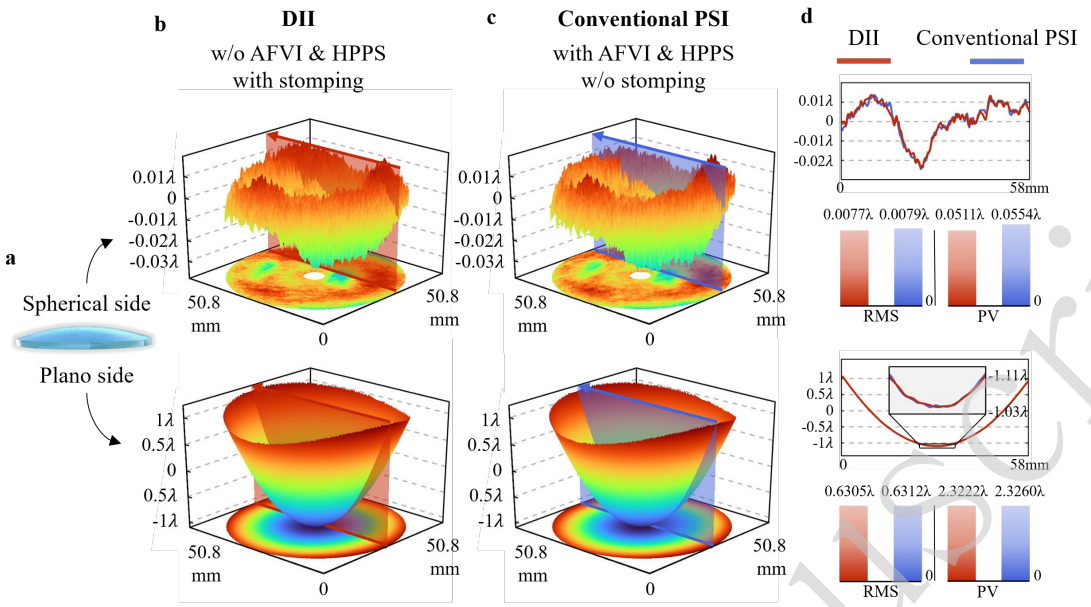

Fig. 6 Comparative measurements of a plano-convex lens. a Test specimen. **b** DII measurement obtained under induced floor stomping conditions, performed without an air-floating vibration isolation platform (AFVI) or high-precision phase shifter (HPPS). **c** Conventional PSI measurement acquired using both AFVI and HPPS in the absence of floor stomping. **d** Comparison of the corresponding surface profiles and associated metrics.

Further robustness validation involved measuring the optical flat crystals under various mechanical disturbances under four experimental conditions (C1–C4). Condition C1 utilised a conventional PSI identical to that in the previous experiment, serving as a baseline reference, with PZT actuation as the phase-shifting source (labelled PZT in Fig. 7). Conditions C2–C4 introduced progressively intensified RMD by turning off the air-floating function of the platform (although residual vibration damping remained from the rubber supports). Disturbances for conditions C2–C4 were intentionally introduced via three distinct mechanisms: floor stomping-introduced vibrations (C2, labelled Stmp in Fig. 7), ballscrew-introduced micro-displacements (C3, labelled Scrw), and stress-induced structural deformation of the supporting platform (C4, labelled Defm). While exact replication of these disturbances is challenging, their effects were precisely quantified by differential phase amplitude (DPA), which increased markedly from C1 (0.2326π rad) to C4 (4.3800π rad).

DII demonstrated outstanding consistency across all conditions (Fig. 7a),

maintaining stable measurements despite increasing the DPA. In contrast, the conventional PSI measurements (Fig. 7b) significantly deteriorated beyond C1, exhibiting pronounced double-carrier frequency errors under moderate disturbances (C2–C3) and completely erroneous results under extreme disturbances (C4).

Measurement repeatability was quantified via RMS wavefront repeatability (RMS-WFR; defined as the mean RMS difference plus twice the standard deviation for the differential between all even-numbered measurements and a synthetic reference (the average of all odd-numbered measurements; calculation was based on 50 sequential measurements). The measurement repeatability remained stable for DII across all conditions (mean RMS-WFR = 0.0017λ), independent of the disturbance intensity. In stark contrast, the RMS-WFR of PSI sharply increased with the disturbance amplitude, peaking at 0.5791λ under C4. This trend was corroborated by additional metrics, as detailed in Supplementary Note 4.

These findings substantiated the effectiveness, precision, and robustness of the DII method under a range of disturbance conditions. For completeness, additional results obtained using a conventional PZT-based configuration without air-floating vibration isolation (AFVI) are provided in Supplementary Note 7. Consequently, we can infer that the DII method is well suited for achieving dependable optical surface topography measurements, even in environments characterised by complex mechanical disturbances.

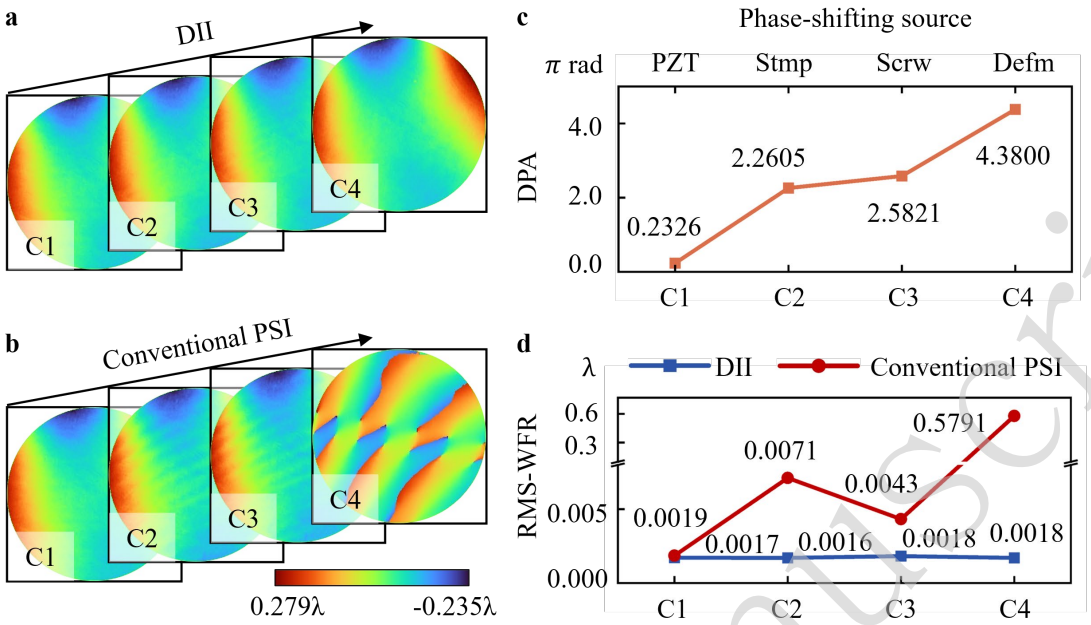

Fig. 7 Surface topography measurements of optical flat crystals under varying conditions. a Surface topography obtained using DII. **b** Surface topography acquired via conventional PSI. **c** DPA recorded under different experimental conditions. **d** Comparison of the RMS wavefront repeatability (RMS-WFR) between DII and conventional PSI across the tested conditions. The phase-shifting sources in C1–C4 are labelled as PZT, Stmp, Scrw, and Defm, corresponding to PZT actuation, floor stomping, ballscrew-introduced micro-displacements, and stress-induced structural deformation of the supporting platform, respectively.

Discussion

To address the longstanding reliance on rigorous vibration isolation and phase control inherent in conventional PSI, our paper introduces and demonstrates a method called DII. DII departs from conventional paradigms by reconceptualising random mechanical disturbances as beneficial excitation signals rather than detrimental noise. By leveraging RMDs and employing the NPDA, our method achieves nanometric precision surface-topography measurements without additional hardware.

The robustness of DII is its most significant advantage. Numerical simulations directly comparing the methods under a strong disturbance (DPA = 7π rad) show that DII achieved a remarkable RMSE of just 0.0005λ, whereas conventional four-step PSI

completely failed, yielding an RMSE of 0.5λ. Numerical simulations revealed that DII exhibits robustness to nonlinear disturbances over a wide range of DPAs, from 0.01π rad to 12π rad, sustaining a solution success rate above 90% throughout. Experimentally, DII achieved an RMS wavefront repeatability below 0.0018 λ in uncontrolled, vibration-prone environments, closely matching the performance of conventional PSI conducted under strictly controlled conditions, with RMS differences as low as 0.0002 λ for spherical surfaces and 0.0007 λ for planar surfaces.

Regarding the computational cost, the NPDA is built upon well-established numerical techniques, including the CZT for coarse estimation and LM method for iterative refinement, which are efficient and widely used. For a representative dataset of ten interferograms at 512 × 512 pixels, the algorithm was completed in approximately 5 s using MATLAB on a standard laptop computer (12th Gen Intel Core i7-12700H, 16 GB RAM). Using basic code-level optimisations in C++, the processing time was further reduced to less than 1 s. These timescales are within practical requirements of surface metrology applications. Further optimisation remains in practice, and an additional discussion of the computational cost, memory usage, and implementation strategies is provided in Supplementary Note 8. In principle, refinement requires at least three frames. In the simulations reported herein, 10 frames were used as a representative case. However, in practical measurements, a larger number of high-quality frames with sufficient phase diversity is generally preferred for a more reliable reconstruction. Another practical hardware boundary is that the disturbance state should remain approximately constant during exposure to a single camera. Accordingly, the disturbance-induced phase variation within one exposure must remain sufficiently small for each interferogram to be treated as a quasistatic frame. Therefore, the maximum tolerable disturbance frequency depends jointly on the exposure time and disturbance amplitude; otherwise, motion blurring or jelly effect distortions appear.

Despite these promising results, several challenges remain to be addressed. This

study focused on mechanical rigid-body disturbances between the test and reference surfaces, which are represented in the current model by frame-dependent piston and tilt terms. In contrast, turbulent airflow introduces phase errors through refractive-index fluctuations in the optical path rather than through rigid-body motion of the optics; therefore, it lies outside the present scope. Its influence on measurement accuracy remains to be investigated in future studies. The applicability range of Eq. (2) should also be noted. The current linear disturbance model is appropriate for planar and low-NA spherical surfaces. For high-NA spherical measurements, additional terms associated with $\sqrt{1-\rho^2 NA^2}$ (where ρ is the normalized coordinate, and NA is the numerical aperture) must be included, requiring corresponding extensions of the model and reconstruction procedure. Moreover, extending the approach to accommodate non-spherical or freeform surface measurements is a compelling direction for future research. In current sub-aperture stitching strategies for non-spherical interferometry, nanometre-scale perturbations between sub-apertures fundamentally limit stitching precision. The adaptive detection capability of DII for such minute disturbances suggests its potential to surmount these limitations. More broadly, the present framework is not inherently restricted to Fizeau geometry. In principle, it can be extended to other PSI-compatible interferometer architectures, such as Twyman–Green and Mach–Zehnder systems, for continuous-wavefront measurements including surface form, wavefront aberration, thickness variation, bow, and warp, provided that an appropriate interferometric forward model is available. However, in its current form, the method is intended for smooth and continuous phase objects. Therefore, it is not directly suitable for rough surfaces, abrupt discontinuities, or complex micro-/nano-structured samples without substantial modifications to both the optical model and the reconstruction algorithm.

Additionally, because the interference model is invariant under simultaneous sign inversion of all phase terms, the NPDA resolves inter-frame sign consistency but cannot determine the absolute orientation of the measured surface (i.e. whether the

reconstruction corresponds to $+\varphi$ or $-\varphi$) from the intensity data alone. In practice, this can be resolved by prior knowledge, such as the known concavity of the test surface or by knowledge of the disturbance direction in at least one frame. This technique also holds considerable promise for integration with common hardware components, such as stepper motors, whose known actuation direction would additionally resolve the absolute sign ambiguity. This would enable more controlled and automated surface topography measurements without the cumbersome hardware characteristics of traditional PSI.

Conclusion

1. In this paper, we propose and demonstrate disturbance-introduced interferometry (DII), in which ambient mechanical disturbances are used as the phase-shifting source, and a natural phase decoding algorithm reconstructs the surface topography from disturbance-modulated interferograms. Numerical and experimental results showed that DII maintains a high measurement accuracy under disturbance conditions, where conventional phase-shifting interferometry degrades severely.

2. The main advantage of the DII is that it reduces the dependence of high-precision interferometric metrology on stringent vibration isolation and precisely controlled phase-shifting hardware. This makes the method particularly attractive for large-aperture optical testing and in situ measurements in vibration-prone manufacturing environments.

3. Future research will extend the present framework beyond the current disturbance model and application scope, including the influence of turbulent airflow, measurement of nonspherical or freeform surfaces, and more general strategies for resolving absolute sign ambiguity.

Acknowledgements. The authors would like to acknowledge the financial support for this work from the National Natural Science Foundation of China (62375171, 62305208, 62405182, 52127801, 52475563), the Key Research Program of the Chinese Academy of Sciences under Grant RCJJ1452403, the Oceanic Interdisciplinary Program of Shanghai Jiao Tong University (SL2022ZD205), the Science and Technology Commission of Shanghai Municipality (20DZ2220400), Shanghai Innovation Action Plan Project (24ZR1492200), and the Startup Fund for Young Faculty at SJTU (24X010500120).

Author contributions. J.Y. conceived the main concept. L. Li and R.X. developed the NPDA, performed simulations, and analysed the data. L. Li designed and built the experimental setup and conducted the measurements. L. Lei contributed to the analysis of the proposed method, provided experimental resources and helped with the validation of the measurement results. Y.H. and X.L. contributed to proof-of-concept experiments, optical system alignment, and data acquisition. L.D., Y.P. and Y.J. assisted with experimental setup construction, algorithm testing, and data processing. Y.S. contributed to simulation design. S.H. provided experimental resources and helped with the validation of the measurement results. J.Y. and S.L. supervised the study. L. Li and R.X. wrote the original draft, and J.Y., L. Lei, S.H., and S.L. reviewed the manuscript.

Data availability. The data that support the findings of this study are available from the authors on reasonable request; see author contributions for specifics.

Conflict of interest. The authors declare no competing interests.

References

1. Sederberg, S. et al. Vectorized optoelectronic control and metrology in a semiconductor. *Nature Photonics* **14**, 680-685 (2020).
2. Khonina, S. N. et al. Analysis of the wavefront aberrations based on neural networks processing of the interferograms with a conical reference beam. *Applied Physics B* **128**, 60 (2022).
3. Osten, W. Optical metrology: the long and unstoppable way to become an outstanding measuring tool. Proceedings of SPIE 10834, Speckle 2018: VII International Conference on Speckle Metrology. Janów Podlaski, Poland: SPIE, 2018, 1083402.
4. Orji, N. G. et al. Metrology for the next generation of semiconductor devices. *Nature Electronics* **1**, 532-547 (2018).
5. de Groot, P. Phase shifting interferometry. in Optical Measurement of Surface Topography (ed Leach, R.) (Berlin Heidelberg: Springer, 2011), 167-186.
6. Lai, G. M. & Yatagai, T. Generalized phase-shifting interferometry. *Journal of the Optical Society of America A* **8**, 822-827 (1991).
7. Marrugo, A. G., Gao, F. & Zhang, S. State-of-the-art active optical techniques for three-dimensional surface metrology: a review [Invited]. *Journal of the Optical Society of America A* **37**, B60-B77 (2020).
8. Strojnik, M., Paez, G. & Mantravadi, M. Lateral shear interferometers. in Optical Shop Testing 3rd edn (ed Malacara, D.) (Hoboken: Wiley, 2007), 122-184.
9. Schober, C. et al. Tilted Wave Fizeau Interferometer for flexible and robust asphere and freeform testing. *Light: Advanced Manufacturing* **3**, 48 (2022).
10. de Groot, P. J. A review of selected topics in interferometric optical metrology. *Reports on Progress in Physics* **82**, 056101 (2019).
11. Liu, Q. et al. Simultaneous dual-wavelength phase-shifting interferometry for surface topography measurement. *Optics and Lasers in Engineering* **124**,

105813 (2020).

12. Freschi, A. A. & Frejlich, J. Adjustable phase control in stabilized interferometry. *Optics Letters* **20**, 635-637 (1995).
13. Zhao, C. Y. & Burge, J. H. Vibration-compensated interferometer for surface metrology. *Applied Optics* **40**, 6215-6222 (2001).
14. Ferrari, J. A. et al. Robust interferometer with external phase-shift control. *Optics Express* **25**, 29965-29970 (2017).
15. Lu, Q. J. & Han, S. Optical surface measurements of a wavelength-tuned Fizeau interferometer based on an optical power, real-time feedback and compensation system. *Results in Physics* **16**, 102846 (2020).
16. Guo, T., Guo, X. Y. & Wei, Y. Y. Multi-mode interferometric measurement system based on wavelength modulation and active vibration resistance. *Optics Express* **29**, 36689-36703 (2021).
17. Hegyi, A. & Martini, J. Hyperspectral imaging with a liquid crystal polarization interferometer. *Optics Express* **23**, 28742-28754 (2015).
18. Zhang, Y., Tian, X. B. & Liang, R. G. Fringe-print-through error analysis and correction in snapshot phase-shifting interference microscope. *Optics Express* **25**, 26554-26566 (2017).
19. Beitia, C. Challenges in Nanotopography measurements at die level. in Frontiers of Characterization and Metrology for Nanoelectronics (eds Secula, E. M. & Seiler, D. G.) (Gaithersburg: NIST, 2017), 63-66.
20. Xu, Y. Y. et al. Derivative method for dual-wavelength three-frame phase-shifting interferometry. *Optik* **226**, 165953 (2021).
21. Li, J. X. et al. All-optical complex field imaging using diffractive processors. *Light: Science & Applications* **13**, 120 (2024).
22. Bobroff, N. Residual errors in laser interferometry from air turbulence and nonlinearity. *Applied Optics* **26**, 2676-2682 (1987).
23. de Groot, P. J. Vibration in phase-shifting interferometry. *Journal of the Optical Society of America A* **12**, 354-365 (1995).

24. de Groot, P. Principles of interference microscopy for the measurement of surface topography. *Advances in Optics and Photonics* **7**, 1-65 (2015).

25. Zhang, L. W. et al. Review of anti-vibration technology in phase-shifting interferometry. *Laser & Optoelectronics Progress* **60**, 1900005 (2023).

26. Cui, X. Q. et al. An improved approach for minimizing the vibrational effects on the phase-shifting interferometry measurement by optimizing the exposure time. *Measurement* **250**, 117062 (2025).

27. McDonnell, E. M. & Deck, L. L. Solutions for environmentally robust interferometric optical testing. Proceedings of SPIE 11487, Optical Manufacturing and Testing XIII. Online Only: SPIE, 2020, 114870J.

28. Cui, W. H. et al. Stability of air floating optical platform based on optimal tuned liquid column damper. *Acta Optica Sinica* **41**, 2122001 (2021).

29. Doloca, R. & Tutsch, R. Vibration induced phase-shift interferometer. Proceedings of SPIE 6292, Interferometry XIII: Techniques and Analysis. San Diego, CA, USA: SPIE, 2006, 62920Y.

30. Martin, H., Wang, K. W. & Jiang, X. Q. Vibration compensating beam scanning interferometer for surface measurement. *Applied Optics* **47**, 888-893 (2008).

31. Tereschenko, S. et al. Passive vibration compensation in scanning white-light interferometry. *Applied Optics* **55**, 6172-6182 (2016).

32. Zhao, W. Q. et al. Research on high-precision large-aperture laser differential confocal-interferometric optical element multi-parameter measurement method. *Light: Advanced Manufacturing* **5**, 47 (2024).

33. Robledo-Sanchez, C. et al. Phase-shifting interferometry based on the lateral displacement of the light source. *Optics Express* **21**, 17228-17233 (2013).

34. Meneses-Fabian, C. et al. Common-path phase-shifting interferometer with binary grating. *Optics Communications* **264**, 13-17 (2006).

35. Navarro-Ahuatl, M. A., Meneses-Fabian, C. & Flores-Meneses, C. A. Automated phase-visibility modulating interferometry. *Optics and Lasers in Engineering* **183**, 108498 (2024).

36. Miao, X. Y. et al. Problems on polarization aberrations in large aperture dynamic interferometry based on the polarization phase shifting technique. *Optics Express* **30**, 35759-35775 (2022).

37. Wolfe, C. R. et al. Measurement of wavefront structure from large-aperture optical components by phase-shifting interferometry. Proceedings of SPIE 2536, Optical Manufacturing and Testing. San Diego, CA, USA: SPIE, 1995, 13-37.

38. Takeda, M., Ina, H. & Kobayashi, S. Fourier-transform method of fringe-pattern analysis for computer-based topography and interferometry. *Journal of the Optical Society of America* **72**, 156-160 (1982).

39. Bone, D. J., Bachor, H. A. & Sandeman, R. J. Fringe-pattern analysis using a 2-D Fourier transform. *Applied Optics* **25**, 1653-1660 (1986).

40. Sugiyama, M. et al. Single-shot surface profiling by local model fitting. *Applied Optics* **45**, 7999-8005 (2006).

41. Tang, L. et al. High-precision large-aperture single-frame interferometric surface profile measurement method based on deep learning. *International Journal of Extreme Manufacturing* **7**, 055601 (2025).

42. Deck, L. L. Model-based phase shifting interferometry. *Applied Optics* **53**, 4628-4636 (2014).

43. Wang, Z. Y. & Han, B. Advanced iterative algorithm for randomly phase-shifted interferograms with intra- and inter-frame intensity variations. *Optics and Lasers in Engineering* **45**, 274-280 (2007).

44. Wang, Z. Y. & Han, B. Advanced iterative algorithm for phase extraction of randomly phase-shifted interferograms. *Optics Letters* **29**, 1671-1673 (2004).

45. Zhang, Y., Tian, X. B. & Liang, R. G. Timesaving phase retrieval approach based on difference map normalization and fast iterative algorithm. *Optics and Lasers in Engineering* **121**, 18-28 (2019).

46. Duan, M. L. et al. Phase-tilt iteration: accurate and robust phase extraction from random tilt-shift interferograms. *Optics and Lasers in Engineering* **142**, 106595 (2021).

47. Kihm, H. Phase recovery of high numerical-aperture spherical surfaces in tilt phase-shift interferometry. *Optical Engineering* **55**, 074101 (2016).

48. Chen, Y. C. & Qian, K. M. General iterative algorithm for phase-extraction from fringe patterns with random phase-shifts, intensity harmonics and non-uniform phase-shift distribution. *Optics Express* **29**, 30905-30926 (2021).

49. Hibino, K. et al. Phase-shifting algorithms for nonlinear and spatially nonuniform phase shifts. *Journal of the Optical Society of America A* **14**, 918-930 (1997).

50. Zhang, Z. et al. Non-iterative phase tilt interferometry for the tilt shift calculation and phase extraction. *Optics Express* **31**, 21239-21252 (2023).

51. Chen, Y. C. et al. Iterative phase-shifting algorithm immune to random phase shifts and tilts. *Applied Optics* **52**, 3381-3386 (2013).

52. Guo, H. W. & Zhang, Z. H. Phase shift estimation from variances of fringe pattern differences. *Applied Optics* **52**, 6572-6578 (2013).

53. Meneses-Fabian, C. & Tejeda-Muñoz, N. Self-calibrating phase-shifting interferometry of three unequal phase steps by fitting background light to a polynomial of degree *K*. *Applied Optics* **56**, 4278-4283 (2017).

54. Ding, H. F. & Guo, H. W. Estimating phase shifts from three fringe patterns by use of cross spectrum. *Applied Optics* **56**, 916-927 (2017).

55. Marquardt, D. W. An algorithm for least-squares estimation of nonlinear parameters. *Journal of the Society for Industrial and Applied Mathematics* **11**, 431-441 (1963).